# A SPICE Compact Model for Ambipolar 2D-Material FETs aiming at Circuit Design

Sheikh Aamir Ahsan, *Member, IEEE*, Shivendra Kumar Singh, Mehak Ashraf Mir, Marta Perucchini, Dmitry K. Polyushkin, Thomas Mueller *Senior Member, IEEE*, Gianluca Fiori, *Senior Member, IEEE*, and Enrique G. Marin

***Abstract*—We report a charge-based analytic and explicit compact model for field effect transistors (FETs) based on two-dimensional materials (2DMs), for the simulation of 2DM-based analog and digital circuits. The device electrostatics is handled by invoking 2D density of states and Fermi-Dirac statistics, that are later combined with Lambert-W function and Halley's correction, so to eventually obtain explicit expressions for the electron and hole charges, which are exploited in the calculation of drift-diffusion currents for both carriers. Further, the charge model is extended to obtain characteristics of 2DM-based negative capacitance FETs. The model is benchmarked against experimental $MoS_2$ FET measurements, and experimental ambipolar characteristics of narrow band-gap materials such as black phophorous. Its soundness for SPICE circuit-level simulations is also demonstrated.**

***Index Terms*—2D Materials, field effect transistor, circuit and compact modeling, SPICE, Verilog-A**

## I. Introduction

In the quest for extending Moore's law, the past decade and a half has seen tremendous research efforts in nanotechnology towards field effect transistors (FETs) based on two-dimensional materials (2DMs). Some of them as graphene, transition metal dichalcogenides, black phosphorus, silicene or germanene have already been employed in FETs [1–6] and are currently investigated as potential alternatives to silicon and III-V technologies [7].

This work was supported in part by the Science and Engineering Research Board through Startup Research Grant under Grant SRG/2019/001122, in part by the European Research Council through the PEP2D Project under Contract 770047, and in part by the European Commission through the Graphene Flagship Core 3 under Contract 881603 and through the ORIGENAL H2020 Project under Contract 863258. The work of Enrique G. Marin was supported by Juan de la Cierva Incorporación [Ministerio de Ciencia e Innovación (MICIIN)/Agencia Estatal de Investigación (AEI)] under Grant IJCI-2017-32297. Corresponding author: Sheikh Ahsan Ahsan.

S. A. Ahsan, S. K. Singh and M. A. Mir are with the Nanoelectronics Research and Development Lab, Department of Electronics and Communication Engineering, National Institute of Technology Srinagar, Srinagar, JK, 190006, e-mail: sheikh@nitsri.ac.in

M. Perucchini and G. Fiori are with the Dipartimento di Ingegneria dell'Informazione, Università di Pisa, Pisa, Italy, e-mail: martaperucchini@me.com, gfiori@mercurio.iet.unipi.it

D. K. Polyushkin and T. Mueller are with the Vienna University of Technology, Institute of Photonics, Vienna, Austria, e-mail: thomas.mueller@tuwien.ac.at

E. G. Marin is with the Dipartimento di Ingegneria dell'Informazione, Universit`a di Pisa, Pisa, Italy, and also with Departamento de Electr´onica, Universidad de Granada, Granada, Spain e-mail: egmarin@go.ugr.es

However, in order to bring 2DMs into electronics circuits [8], [9] and, therefore, to eventually achieve industrial applications, circuit designers need Process Design Kits built around device compact models. These core models must essentially be fast, accurate, robust and, more importantly, must preserve the underlying physics of device operation, so to better predict and rationalize the experimental device characteristics [10]. In order to attain this objective, several models for 2DM-FETs have been proposed in the literature, both in the ballistic and in diffusive regimes.

In the former case, most of the works [11–13] rely on Landauer's formalism for calculating the device current [14]. However, by employing Landauer's integral function, they only obtain a closed-form expression for the current under near-equilibrium conditions and have, therefore, a limited bias validity. Moreover, these models are appropriate for ultra-short transistors (where the channel length is smaller than the scattering mean-free-path), but the state-of-the-art in 2DMs synthesis is still far from this regime, and 2DM-based transistors are still better explained in a drift-diffusive approximation.

In this latter regime, the works in Refs. [15–17] are relevant in terms of being either explicit or SPICE compatible. However, they are funded on the Boltzmann approximation (so to simplify the model derivation) and neglect Fermi-Dirac (FD) statistics, essential for handling the electrostatics in 2DMs. Another set of 2DM-FETs models proposed in Refs. [18–25] do consider FD statistics, but they are either implicit or iterative in nature [18–22] or they lack the capability of dealing with ambipolar current characteristics [21–26]. Elsewhere, of the two SPICE compatible ambipolar 2DM-FET models in Refs. [27], [28], the model discussed in Ref. [27] is phenomenological in nature, whereas Ref. [28] uses variable range hopping and trap-release mechanisms for modeling carrier transport.

In this work, which leverages the results presented by some of the authors in Ref. [29], we build an ambipolar 2DM-FET compact model, with explicit expressions for electron and hole charges and currents, suitable for SPICE circuit simulation and including also negative capacitance (NC) effects; we compare and validate it against in-house experimental results of a monolayer $MoS_2$ FET, and also with $MoTe_2$ and black-phosphorous results from the literature. The model while being suitable for long-channel devices, handles 2DM-based devices with drift-diffusive transport and can work for channel lengths as short as 100 nm since most of 2DMs e.g $MoS_2$, black phosphorus etc. have mean free paths of the order of few tens of nanometers [23], [30], thereby making drift diffusion as the appropriate approach to describe carrier transport.

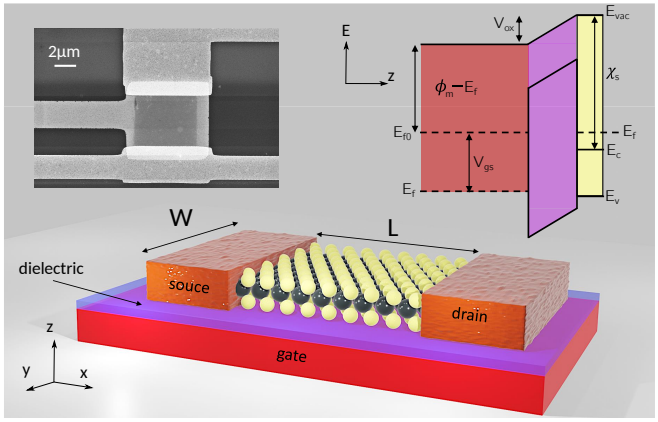


Fig. 1: Schematic representation of the 2DM-FET and band-diagram taken along the gate/insulator/2DM direction at any point $x$ in the channel for an applied gate-to-channel potential $V_{g-ch}$. $\phi_m$ is the gate metal work function, $\chi_s$ the 2DM electron affinity, that together with donor/acceptor impurity density $N_{\mathrm{d/a}}^{+/-}$, define the threshold voltage $V_T = \phi_{\mathrm{m}}/q - \chi_{\mathrm{s}}/q - qN_{\mathrm{d/a}}^{+/-}/C_{\mathrm{ox}}$, $E_f$ is the Fermi level, and $E_c/E_v$ is the conduction band bottom / valence band top in the 2DM channel. Shown at the top-left is the scanning electron microscope image of an in-house fabricated $MoS_2$ device employed for the experimental comparison.

The remainder of the article is organized as follows: first the model electrostatics and explicit ambipolar charge calculation are discussed, followed by the derivation of the drift-diffusion ambipolar current and by the development of the 2DM-NC-FET model. Next, the model is validated against experimental results, and circuit quality checks and a circuit simulation exemplifying its use is performed. Finally, conclusions are drawn.

## II. Model Electrostatics

In first place, we deal with the formulation of the electrostatics by analysing a vertical cross section of the 2DM-based FET. Figure 1(a) shows a schematic of the device with source / drain contacts patterned at the top of 2DM ultra-thin layer, which is separated from the metallic back-gate through a dielectric.

The band diagram for the structure along the $z$ direction (at any position $x$) is sketched in Fig. 1(b) where the equation for to the potential (that includes both the electron ($n$) and hole ($p$) charge densities) reads [29]

$$\frac{q^2}{C_{\mathrm{ox}}}(n-p) + E_f - E_c = qV_{gs} - qV_T \tag{1}$$

where $n$ and $p$ are, indeed, determined by the 2DM density of states for electron/holes ($D_n$ and $D_p$, respectively) and by Fermi-Dirac statistics, so that: $n = D_{\mathrm{n}}kT\ln\left[1+\exp\left((E_f-E_c)/kT\right)\right]$ and $p = D_{\mathrm{p}}kT\ln\left[1+\exp\left((E_v-E_f)/kT\right)\right]$; $k$ is the Boltzmann constant, $T$ the temperature, $E_f$ the Fermi level, $E_c/E_v$ the conduction band bottom/valence band top in the 2DM channel, and $V_T$ the threshold voltage.

It must be noted that for a non-equilibrium scenario, the quantities $n$, $p$, $E_c$, $E_v$ and $E_f$ become functions of position along the channel. Moreover, the Fermi level splits into quasi-Fermi levels for electrons and holes ($E_{fn}$ and $E_{fp}$). Thus, from the carrier statistics of electron and holes the following relations for the position-dependent non-equilibrium pseudo-Fermi levels and band edges can be obtained:

$$E_{fn}(x) - E_c(x) = kT\ln\left[\exp\left(\frac{n(x)}{D_nkT}\right) - 1\right] \tag{4}$$

$$E_v(x) - E_{fp}(x) = kT\ln\left[\exp\left(\frac{p(x)}{D_pkT}\right) - 1\right] \tag{5}$$

After some algebra and summing up the former expressions we reach the charge-control equation out-of-equilibrium including both types of carriers:

$$e^{(E_{fn}(x)-E_{fp}(x)-E_g)/kT} = \left(e^{n(x)/D_nkT}-1\right)\left(e^{p(x)/D_pkT}-1\right) \tag{6}$$

which relates $n$ and $p$ with the semiconductor bandgap, $E_g$, and the electron-hole quasi-Fermi-level splitting, $E_{fn} - E_{fp}$. Together, Eqs. (2-6) can be used to express $n$ in terms of $p$, and vice versa, as:

$$n(x) = D_nkT\ln\left(1 + \frac{e^{(E_{fn}(x)-E_{fp}(x)-E_g)/kT}}{e^{p(x)/D_pkT}-1}\right), \tag{7}$$

$$p(x) = D_pkT\ln\left(1 + \frac{e^{(E_{fn}(x)-E_{fp}(x)-E_g)/kT}}{e^{n(x)/D_nkT}-1}\right). \tag{8}$$

For the non-equilibrium scenario a corresponding change in the original potential balance expression in Eq (1) needs to be made by replacing $V_{gs}$ by $V_{g-ch}$, where the latter represents the gate-to-channel potential. Indeed, $V_{g-ch} = qV_{g-s} - qV_{ch-s}$, where $qV_{ch-s} = E_{fn(p)}(x) - E_{f,s}$ and the source Fermi-level, $E_{f,s}$, is unique for electron and holes (assuming ideal contacts) and can be taken as reference for energies, i.e $E_{f,s} = 0$. Using the above updates for non-equilibrium along the channel, together with Eqs. (1), (7), and (8) results in the pair of charge control equations for electrons and holes given in (2) and (3) at the bottom of this page, where the position dependent argument $(x)$ has been omitted here for the sake of clarity.

It can be observed that Eqs. (2) and (3) are transcendental in nature and have to be solved self-consistently for each bias point, therefore turning the model in computationally expensive. In order to make it explicit, fast and compatible

$$\frac{q^2}{C_{\mathrm{ox}}}\left[n - D_pkT\ln\left(1+\frac{e^{(E_{fn}-E_{fp}-E_g)/kT}}{e^{n/D_nkT}-1}\right)\right] + kT\ln\left(e^{n/D_nkT}-1\right) = q\left(V_{gs}-V_T\right) + E_{fn}, \tag{2}$$

$$\frac{-q^2}{C_{\mathrm{ox}}}\left[p - D_nkT\ln\left(1+\frac{e^{(E_{fn}-E_{fp}-E_g)/kT}}{e^{p/D_pkT}-1}\right)\right] - kT\ln\left(e^{p/D_pkT}-1\right) = q\left(V_{gs}-V_T\right) + E_{fp} + E_g \tag{3}$$

with circuit-level simulations, we explore the possibility to rewrite electron and hole charges in the form $y = ze^z$ to arrive at a solution $z = W(y)$ where $W$ represents the Lambert-W function [31], [32], which can further be used to calculate the drift-diffusion current. The $ze^z$ form can be achieved by making the following approximations in Eqs. (2) and (3): *i*) neglect the second term due to the strong negative exponential dependence on $E_g$, *ii*) Taylor expanding $e^{n/n_q}(e^{p/p_q})$ as $1+n/n_q$ $(1+p/p_q)$ under low carrier concentration conditions in the channel. This facilitates the initial guess calculation for electron ($n_0$) and hole ($p_0$) charges as:

$$n_0 = n_b \times W\left(\frac{n_q}{n_b} e^{(V_{gs}-V_T+E_{fn})/\phi_{th}}\right) \tag{9}$$

$$p_0 = p_b \times W\left(\frac{p_q}{p_b} e^{-(V_{gs}-V_T+E_{fp}+E_g)/\phi_{th}}\right) \tag{10}$$

where we have introduced the following characteristic carrier concentrations: $n_q/p_q = D_{n/p}kT$ and $n_b = p_b = C_{ox}\phi_{th}/q$ that are associated to the 2DM and oxide properties, respectively.

In order to minimize the error introduced by Taylor expansion, and extend the validity of this initial guess under a broad range of bias conditions, we refine it using the Halley's method [33], [34] (later checked in Section 6(d)) so that $n = n_0 + \Delta_n$ and $p = p_0 + \Delta_p$ where:

$$\Delta_{n(p)} = -\frac{r_{n(p)}}{r^{'}_{n(p)}}\left(1 + \frac{0.5 r_{n(p)} r^{''}_{n(p)}}{{r^{'}_{n(p)}}^2}\right) \tag{11}$$

Here, $r^{'}_{n(p)}$ and $r^{''}_{n(p)}$ denote the first and second derivatives of $r_{n(p)}$ respectively with respect to the initial guess $n_0$ ($p_0$), gathered at the bottom of the page in (12) and (13).

## III. Ambipolar Drift-Diffusion Current Model

Next, we discuss the device current characteristics. Within the drift-diffusion formalism, the ambipolar current density can be expressed as:

$$\frac{I}{W} = J = J_n + J_p = -\mu_n n\frac{dE_{fn}}{dx} - \mu_p p\frac{dE_{fp}}{dx} = -\mu_n n\frac{dE_{fn}}{dn}\frac{dn}{dx} - \mu_p p\frac{dE_{fp}}{dp}\frac{dp}{dx} \tag{14}$$

where $\mu_{n/p}$ denotes the electron/hole mobility. Invoking current continuity the above equation can be integrated along the channel length. The limits $x = 0$ at source and $x = L$ at drain, are translated into $n_s$/$p_s$ and $n_d$/$p_d$ for electron/hole concentrations at the source and drain, so that:

$$\frac{I}{W}L = -\mu_n \int_{n_s}^{n_d}\left(n\frac{dE_{fn}}{dn}\right)dn - \mu_p\int_{p_s}^{p_d}\left(p\frac{dE_{fp}}{dp}\right)dp \tag{15}$$

For the calculation of $J_n$ one can differentiate Eq. (2) with respect to $n$, while making the approximation $E_{fn}(x) \approx E_{fp}(x)$ [18], so that $dE_{fn}/dn$ as:

$$\frac{dE_{fn}}{dn} = \frac{kT}{n_b} + \frac{kT}{n_q}\frac{e^{n/n_q}}{e^{n/n_q}-1} + \frac{kT}{n_b}\frac{p_q}{n_q}\left[\frac{e^{n/n_q}}{e^{n/n_q}-1} \times \frac{1}{1+e^{E_g/kT}\left(e^{n/n_q}-1\right)}\right] \tag{16}$$

Using the change of variable $u = n/n_q$, $J_n$ is written as:

$$J_n = -\mu_n \frac{n_q^2 kT}{L}\int_{u_s}^{u_d}\left[\frac{u}{n_b} + \frac{u}{n_q}\frac{e^u}{e^u-1} + \frac{u}{n_b}\frac{p_q}{n_q}\left(\frac{e^u}{e^u-1} \times \frac{1}{1+e^{E_g/kT}\left(e^u-1\right)}\right)\right]du \tag{17}$$

that can be processed following a similar procedure as detailed in Ref. [29], yielding:

$$J_n = -\mu_n \frac{n_q^2 kT}{L}\Bigg[\left(\frac{u^2}{2n_b}\right) + \frac{1}{n_q}\left(1+\frac{p_q}{n_b}\right)\left[u\ln\left(e^u-1\right)\right] - \frac{p_q}{n_q n_b}\left[u\ln\left(1+e^{E_g/kT}\left(e^u-1\right)\right)\right] - \frac{1}{n_q}\left(1+\frac{p_q}{n_b}\right)\left(\frac{u^2}{2}+e^{-u}\right) + \frac{p_q}{n_q n_b}\int\ln\left(1+e^{E_g/kT}\left(e^u-1\right)\right)du\Bigg]_{u_s}^{u_d} \tag{18}$$

The same set of steps could be followed to obtain $J_p$, resulting in:

$$J_p = \mu_p \frac{p_q^2 kT}{L}\Bigg[\left(\frac{v^2}{2n_b}\right) + \frac{1}{p_q}\left(1+\frac{n_q}{n_b}\right)\left[v\ln\left(e^v-1\right)\right] - \frac{n_q}{p_q n_b}\left[v\ln\left(1+e^{E_g/kT}\left(e^v-1\right)\right)\right] - \frac{1}{p_q}\left(1+\frac{n_q}{n_b}\right)\left(\frac{v^2}{2}+e^{-v}\right) + \frac{n_q}{p_q n_b}\int\ln\left(1+e^{E_g/kT}\left(e^v-1\right)\right)dv\Bigg]_{v_s}^{v_d} \tag{19}$$

$$r_n = \frac{C_{ox}}{q}\left(V_{gs}-V_T+\frac{E_{fn}}{q}\right) - n_0 + p_q\ln\left(1+\frac{e^{-E_g/kT}}{e^{n_0/n_q}-1}\right) - n_b\ln\left(e^{n_0/n_q}-1\right) \tag{12}$$

$$r_p = \frac{C_{ox}}{q}\left(V_{gs}-V_T+\frac{E_{fp}}{q}\right) + p_0 - n_q\ln\left(1+\frac{e^{-E_g/kT}}{e^{p_0/p_q}-1}\right) + p_b\left[\ln\left(e^{p_0/p_q}-1\right)+\frac{E_g}{kT}\right] \tag{13}$$

where $v = p/p_q$.

Equations (18) and (19) represent the exact charge-based expressions for electron and hole contributions to the drift-diffusion current and can be further simplified by making the following approximations: *i*) for $u \gg 1$, $u\ln(e^u - 1) \approx u^2$ and *ii*) for $u \to 0$, $u \ll 1$, $u\ln(e^u - 1) \approx e^{-u}$. Similar approximations can be made for terms involving $v$, to yield a more compact total current expression:

$$\frac{I}{W} = \mu_p \frac{p_q^2 kT}{L}\left[\left(\frac{v^2}{2n_b}\right) + \frac{1}{p_q}\left(\frac{v^2}{2} - e^{-v}\right)\right]_{v_s}^{v_d} - \mu_n \frac{n_q^2 kT}{L}\left[\left(\frac{u^2}{2n_b}\right) + \frac{1}{n_q}\left(\frac{u^2}{2} - e^{-u}\right)\right]_{u_s}^{u_d} \quad (20)$$

This expression together with the explicit charge equations obtained in the previous section, constitute the core of the compact circuit model for 2DM-based FETs proposed here.

We can further extend the model with non-ideality factors in order to account for non-ideal effects at the contacts such as thermally assisted tunneling or Schottky-barrier lowering by using a modified thermal voltage for electron and holes: $kT_e = kT \times (1 + \eta_e)$ and $kT_h = kT \times (1 + \eta_h)$. This also facilitates a better handling of the sub-threshold characteristics as it is implemented in Ref. [18]. Furthermore, a velocity saturation model in a fashion similar to [27] can also be included for high lateral electric field conditions so to account for current limited by drift saturation velocity as it has been discussed in detail in [35]. The model is, in the following, augmented including the possibility to consider a negative capacitance effect.

## IV. Negative Capacitance Effect

The negative capacitance (NC) effect [36], which results from the insertion of a ferro-electric (FE) material into the gate-oxide stack, has over the last decade been touted as an encouraging option for low-power electronics [37]. In order to model 2DM-based NC-FETs, the main objective is to obtain the voltage across the FE layer ($V_{FE}$) for a given applied $V_{gs}$. Considering the device electrostatic capacitance behaviour one can relate $V_{FE}$ and $V_{gs}$ as: $V_{gs} = V_{FE} + V_{bg}$ where $V_{bg}$ is the back gate voltage. We can further use the Landau-Khalatnikov equation to find $V_{FE}$ in terms of the charge density $Q$ across the FE layer as [38]

$$V_{FE} = 2t_{FE}\alpha_0 Q + 4t_{FE}\beta_0 Q^3 + 6t_{FE}\gamma_0 Q^5 \quad (21)$$

where $t_{FE}$ denotes the FE thickness, and $\alpha_0$, $\beta_0$ and $\gamma_0$ represent the Landau parameters. $Q$ can be calculated in terms of the total gate charge as: $Q = \frac{q}{L}\int_0^L (p - n)\, dx$, and using the expression previously introduced. In particular, if the 2DM-based NC-FET is of unipolar nature, with only the electron branch, this integral can be transformed by integrating with respect to $n$ and by expressing $dx$ in terms of $dn$ as, $dx = (-\mu_n n W/I_n)\,(dE_{fn}/dn)\, dn$. We can further plug in $dE_{fn}/dn$ from Eq. (16) and Taylor expand the exponential terms before performing the integral to finally yield:

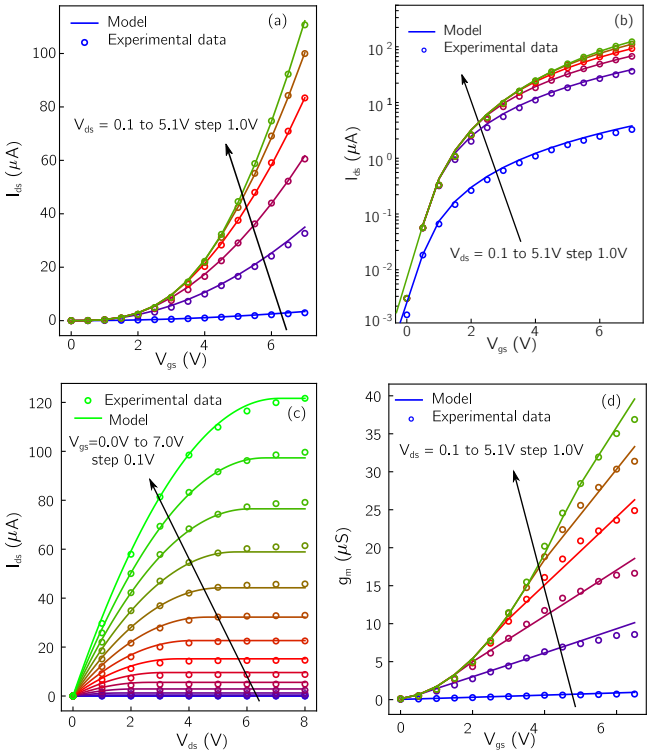


Fig. 2: Comparison of experimental and modelled electrical characteristics for a $MoS_2$ FET for: $I_{ds}$ - $V_{gs}$ in (a) linear and (b) semi-logarithmic scales, (c) $I_{ds}$ - $V_{ds}$ and (d) $g_m$ - $V_{gs}$. The methods are described in detail in [9].

$$Q = qkT\mu_n \frac{W}{L}\left[\left(\frac{1}{n_b} + \frac{1}{n_q}\right)\frac{n^3}{3} + \frac{n^2}{2}\right]_{n_s}^{n_d} \times \frac{1}{I_n}. \quad (22)$$

which is the gate charge needed to determine the ferroelectric voltage.

## V. Results and Discussion

In order to check the predictive capabilities of the 2DM-FET model, we compared the model results with I-V characteristic of an experimental $MoS_2$-based FET. The details of the fabrication process are provided in the methods of Ref. [9]. In particular, in Figure 2 we show the transfer characteristic, i.e. $I_{ds}$ vs. $V_{gs}$, in the (a) linear and the (b) logarithmic scale, as well as the transconductance ($g_m$), and the output characteristics, i.e. $I_{ds}$ vs. $V_{ds}$ for the theoretical (symbols) and experimental (lines) results.

The parameters employed for the comparison are summarized in Table I. The device geometrical parameters are extracted from the experiments and the material constants such as the bandgap, carrier and density of state effective masses, etc., are taken from the literature. Thereafter $N_d^+$, $\phi_m$ and $\chi_s$ are considered as the parameters to match the model against the experimental data in the semi-logarithmic transfer characteristics. Finally, the mobility is adjusted from the transconductance characteristics for near-equilibrium $V_{ds}$ values. As can be seen, the model is able to capture the electrical response of the experimental device in all regimes

TABLE I: List of parameters used for experimental validation

| Parameter | $MoS_2$ | $MoTe_2$ | BP | Parameter | $MoS_2$ | $MoTe_2$ | BP |
|---|---|---|---|---|---|---|---|
| $L$ ($\mu$m) | 5 | 1 | 0.6 | $W$ ($\mu$m) | 20 | 2 | 4 |
| $\epsilon_{ox}(\epsilon_0)$ | 9 | 22 | 22 | $t_{ox}$ (nm) | 30 | 1 | 15 |
| $D_n$ ($10^{14}$/eVcm$^2$) | 2.29 | 2.65 | 6.25 | $D_p$ ($10^{14}$/eVcm$^2$) | - | 3.17 | 5.84 |
| $\phi_m$ (eV) | 4.33 | 3.2 | 3.75 | $\chi_s$ (eV) | 4.31 | 3.19 | 3.5 |
| $N_d^+$ $\times 10^{12}$ /cm$^2$ | 0.001 | 0.1 | 0.1 | $E_g$ (eV) | 1.8 | 1.39 | 0.8 |
| $\mu_e$ (cm$^2$/Vs) | 2 | 11.5 | 81 | $\mu_h$ (cm$^2$/Vs) | - | 24 | 870 |
| $\eta_e$ | - | 1.5 | 1.4 | $\eta_h$ | - | 0.6 | 3.5 |
| Dielectric | $Al_2O_3$ | $HfO_2$ | $HfO_2$ | | | | |

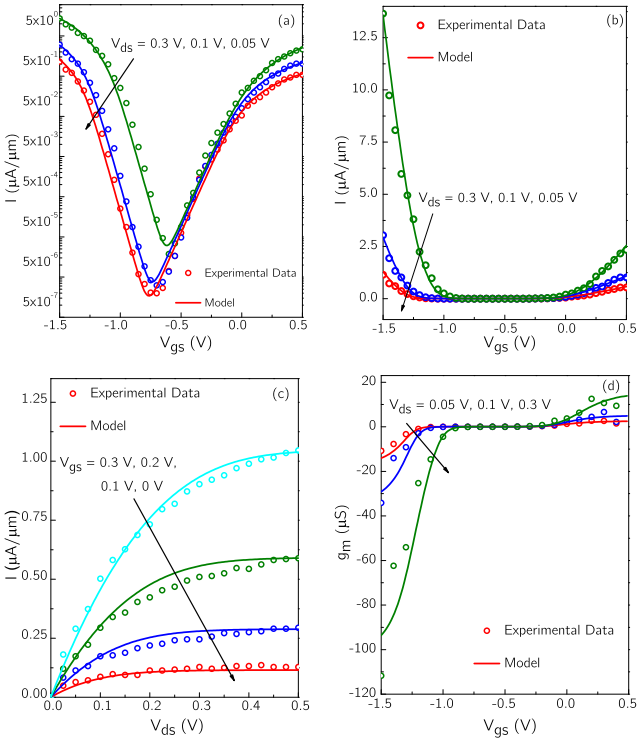


Fig. 3: Comparison of experimental and modeled characteristics for a $MoTe_2$ FET for: $I_{ds}$ - $V_{gs}$ in (a) linear and (b) semi-logarithmic scales, (c) $I_{ds}$ - $V_{ds}$ and (d) $g_m$ - $V_{gs}$. The experimental data has been taken from [40].

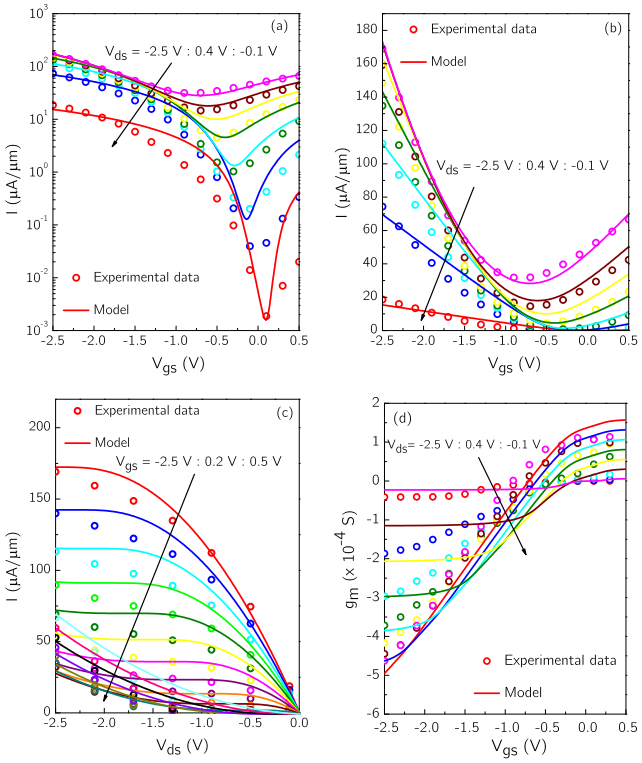


Fig. 4: Comparison of experimental and modeled characteristics for a black-phosphorus FET for: $I_{ds}$ - $V_{gs}$ in (a) linear and (b) semi-logarithmic scales, (c) $I_{ds}$ - $V_{ds}$ and (d) $g_m$ - $V_{gs}$. The experimental data has been taken from [41], [42].

of operation, over four orders of drain current magnitudes, showing a very good agreement for all considered biases.

To further analyse the soundness of the model in an ambipolar scenario, we have also considered the experimental current-voltage characteristics of $MoTe_2$ and black-phosphorous (BP) FETs reported in the literature[40–42]. The modelled and experimental characteristics for $MoTe_2$ and BP devices are shown in Figs. 3 and 4. A very good agreement is achieved not only for transfer (a, b) and output (c) characteristics, but also for the transconductance (d). The physical dimensions of these devices along with the extracted model parameters are detailed in Table I, also including the non-ideality factors $\eta_e$ and $\eta_h$, that are empirical in nature, and are tuned so to properly reproduce the sub-threshold characteristics.

As can be seen, the model captures in detail the ambipolar current both in the transfer and in the output characteristics and also predicts smooth and continuous transconductance. It slightly overestimates the current for the BP device, particularly for the electron branch in the subthreshold region. This could possibly be due to i) trapping of carriers at the interface between the dielectric and the BP channel, not considered in the model, ii) degradation of the experimental carrier mobility as a result of ionized impurity or phonon scattering, also not taken into account in the model. Both effects can, nevertheless, be included into the model, however, at the expense of numerical calculations and ad-hoc fitting models.

We also check the applicability of the model after incorporating the NC effect. In particular, Figure 5 shows the transfer characteristic of a $MoS_2$-NC-FET where a $Hf_{0.5}Zr_{0.5}O_2$ FE layer with $t_{FE} = 20$nm is included in the gate stack [39]. The model is in good agreement with the experimental realization as shown in the (a) linear and (b) semi-logarithmic scales. The Landau parameters used in model fitting are taken from [37].

Finally, for a compact model to be qualified as appropriate

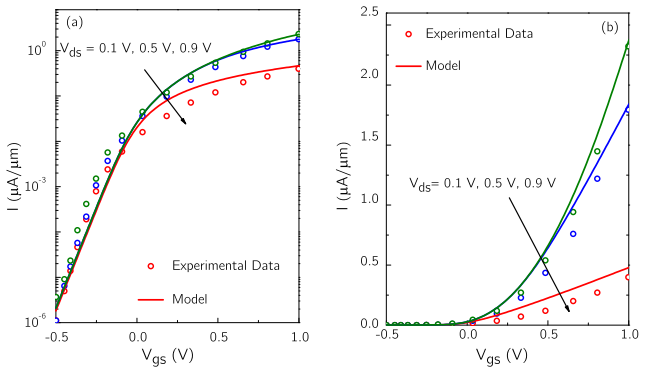


Fig. 5: Comparison of measured and modeled characteristics of a 2D-NC-FET for: (a) $I_{ds}$ - $V_{gs}$ (logarithmic) (b) $I_{ds}$ - $V_{gs}$ (linear). The experimental data has been taken from [39].

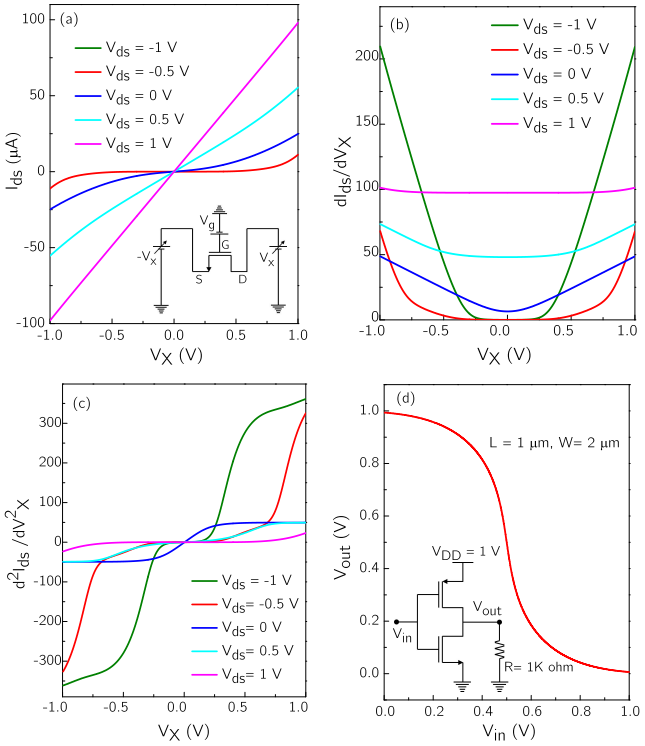


Fig. 6: Gummel Symmetry plots shown for multiple bias conditions for: (a) Gummel current (b) Current First derivative (c) Current Second derivative, highlighting smooth and symmetric characteristics. (d) SPICE simulation for an inverter using the model card extracted for device I in Table I. The model produces well behaved inverter characteristics, thereby advocating the SPICE compatibility of the Verilog-A coded model.

for circuit simulations, certain checks are essential in terms of validation against experimental data. One of such model quality benchmark tests is the well-known Gummel symmetry test [43], that is essential to ensure that the model does not lead to any singularity at $V_{\rm ds} = 0$ V for the I-V characteristics and its higher order derivatives. In circuit applications, where the $V_{ds}$ switches through 0 V its presence may lead to incorrect results. Since we aim to deploy the SPICE model presented in this work for 2D material based circuit design, a well behavior in the Gummel test becomes essential.

Figure 6 shows the results as produced by our model, where highly symmetric, smooth and continuous characteristics are observed for multiple derivatives. After syntactically coding the model in Verilog-A, it is possible to evaluate its circuit-level behaviour for analogue and digital 2DM-based electronics. To exemplify it, a SPICE simulation for an inverter is shown in Fig. 6(d) the model is used for both the p-type and n-type transistors. The model card used is the same as that extracted for the $MoS_2$ FET in Table I.

## VI. Conclusion

A SPICE-compatible charge-based model for 2DM-FETs is presented. It takes into consideration Fermi-Dirac distribution for carrier statistics while handling the electrostatics and uses drift-diffusion for transport. The explicit charge calculation is accomplished by invoking the Lambert-W function along with the Halley's correction. Additionally, the negative capacitance effect is incorporated. It is consistent and predictive when checked with experimental results from fabricated unipolar $MoS_2$ FET, and ambipolar $MoTe_2$ and black phosphorus transistors from literature, illustrating its usability across 2D-material technologies while preserving a meaningful parameter set. The model does not employ any iterative loops or self-consistent solutions, and is analytic yet simple in nature with only a handful of parameters. As such, it is easily deployed in a Verilog-A framework for a quick SPICE circuit simulation while also qualifying the Gummel symmetry test.

## Acknowledgements

Authors gratefully acknowledge the support from Science and Engineering Research Board through Startup Research Grant (Grant no. SRG/2019/001122), European Commission through the Graphene Flagship Core 3 (contract no. 881603) and through the ORIGENAL H2020 Project (contract n. 863258). E.G. Marin also acknowledges Juan de la Cierva Incorporación IJCI-2017-32297 (MINECO/AEI).

## Appendix I - $MoS_2$ FET Fabrication Methods

The $MoS_2$ device is fabricated by means of the electron-beam lithography (Raith e-LINE system) using the resist AR-P 679.04 from Allresist. Metal deposition is carried out in a Leybold electron-beam evaporation system at a pressure of $< 5 \times 10^7$ mbar. The first metal layer defines the gate electrodes and consists of 3nm/30 nm Ti/Au. A 30-nm-thick $Al2O_3$ gate dielectric is then deposited using atomic layer deposition from trimethylaluminium and water at 200° C. The $MoS_2$ films is CVD grown on sapphire substrate and then transferred using a polystyrene (PS) carrier film onto the target substrate in a dry-air glovebox (the PS is subsequently dissolved in toluene). We use Ar/SF6 plasma etching in an Oxford Cobra reactive ion etching system to define the actual transistor channels and electron-beam lithography (Raith e-LINE system). In a final step, we deposit 30 nm of $Au$ to define the source and drain electrode.

From the perspective of electronic circuits, hysteresis is a major obstacle that needs to be overcome in order to implement reliable and operative digital and analog applications. For this reason, in the prediction of the operation of complex

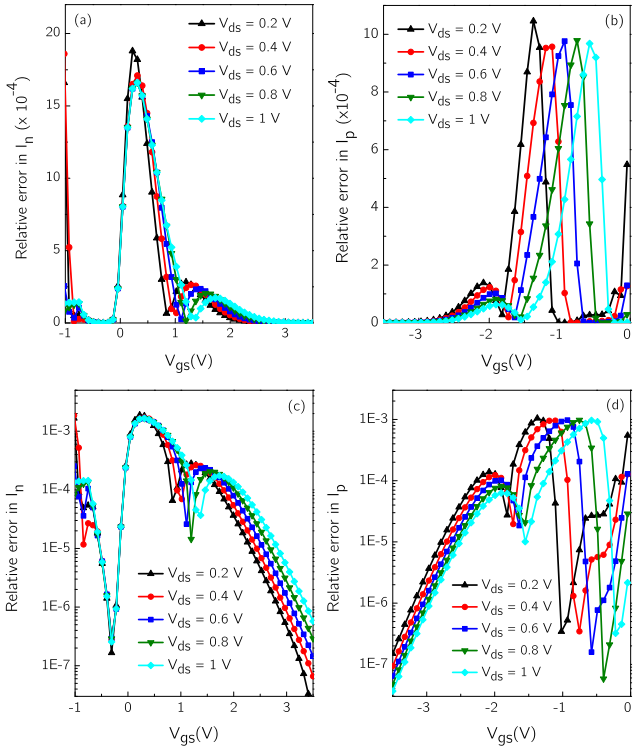


Fig. 7: Relative errors in (a, c) electron and (b, d) hole current components calculated using the explicit charge expressions, with respect to currents obtained from numerical solutions of (2) and (3). Linear plots are shown in (a, b) whereas (c, d) highlight the relative error in logarithmic scale, for multiple bias conditions.

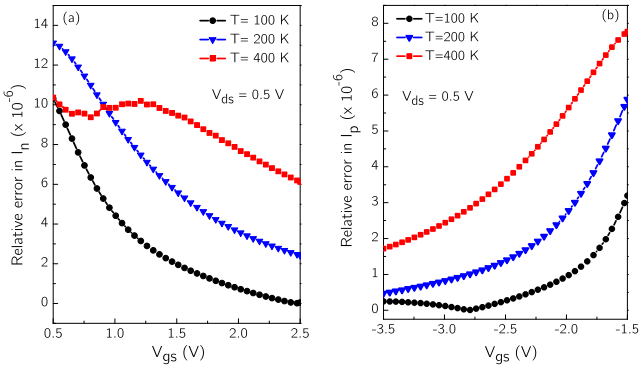


Fig. 8: Relative error in (a) electron and (b) hole current components calculated using the explicit charge expressions, with respect to currents obtained from numerical solutions of (2) and (3) for different temperatures.

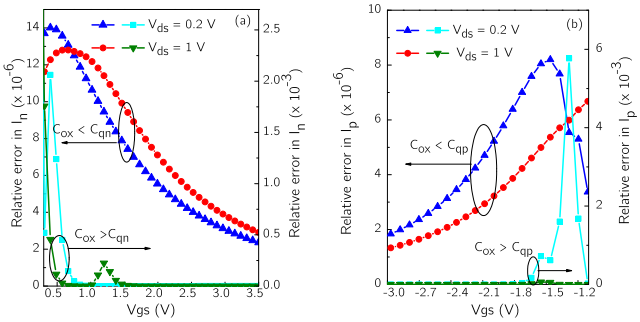


Fig. 9: Relative error in (a) electron and (b) hole current components calculated using the explicit charge expressions, with respect to currents obtained from numerical solutions of (2) and (3) for two different $C_{ox}$ cases, at multiple bias conditions. $C_{qn}$ and $C_{qp}$ denote the degenerate quantum capacitances for electron and hole cases respectively.

electronic circuits in a consolidated technology, which is the purpose of compact modeling, it is mainly considered as a spoiling effect that will be relegated with the advancement of the experimental state of the art and it is typically ignored. In our in-house device case, we achieved a reasonably small hysteresis by taking care of the processing and the materials, whereas the data taken from literature exhibit significantly small hysteresis [40] or no hysteresis at all [41], [42]. The measurements for all the three devices were carried out under vacuum probe stations [9], [40], [42].

## Appendix II - Explicit SPICE Model Accuracy

The accuracy of the explicit expressions for charge, obtained using the Lambert-W function, and its impact on the accuracy of the calculation of the 2DM-FET current is discussed in Fig. 7. A comparison is made against relative error in electron and hole currents, computed using numerical solutions of (2) and (3), and their explicit counterparts, for a wide range of $V_{gs}$ over multiple $V_{ds}$ values. The maximum relative error of the order of $10^{-4}$ to $10^{-3}$ indicates a reasonably good match between the two approaches.

In Fig. 8, the relative error for electron and hole currents is plotted against multiple temperature and bias conditions with relative error of the order of $10^{-6}$ evidencing the robustness of the approach. In Fig. 9, we have considered different scenarios for the oxide and quantum capacitances. A relative error of the order of $10^{-6}$ to $10^{-5}$ is observed for electron and hole currents when $C_q$ dominates $C_{ox}$ and this error order changes to $10^{-4}$ to $10^{-3}$ when $C_{ox}$ dominates $C_q$. We have further observed a range of $C_{ox}$ for which permissible accuracy between the explicit and numerical approaches is obtained. The allowed range obtained is approximately $C_q/25 < C_{ox} < 5C_q$ for both electron and hole cases, where $C_q$ is the quantum capacitance.

## References


[1] M. C. Lemme, T.J. Echtermeyer, M. Baus, and H. Kurz. "A graphene field-effect device," *IEEE Electron Device Letters*, vol 8, no 4, pp. 282. 2007. doi: 10.1109/LED.2007.891668.

[2] B. Radisavljevic, A. Radenovic, J. Brivio, V. Giacometti, and A. Kis. "Single-layer MoS2 transistors," *Nature Nanotechnology*, vol. 6, pp. 147. 2011. doi: 10.1038/nnano.2010.279.

[3] L. Li, Y. Yu, G. J. Ye, Q. Ge, X. Ou, H. Wu, D. Feng, X. Chen, and Y. Zhang, Y. "Black phosphorus field-effect transistors". *Nature Nanotechnology*, vol. 9, p. 372. 2014. doi: 10.1038/nnano.2014.35.

[4] L. Tao, E. Cinquanta, D. Chiappe, C. Grazianetti, M. Fanciulli, M. Dubey, A. Molle, and D. Akinwande. "Silicene field-effect transistors operating at room temperature," *Nature Nanotechnology*, vol. 9, p. 227. 2017. doi: 10.1038/nnano.2014.325.

[5] S. Das, M. Demarteau, and A. Roelofs, "Ambipolar Phosphorene Field Effect Transistors," *ACS Nano*, vol. 8(11), pp. 11730-11738. 2014. doi: 10.1021/nn505868h.

[6] B.N. Madhushankar, A. Kaverzin, T. Giousis, G. Potsi, D. Gournis, P. Rudolf, G. R. Blake, C.H. Van Der Wal, and B. J. Van Wees. "Electronic properties of germanane field-effect transistors". *2D Materials*, vol. 4, p. 021009. 2017. doi:10.1088/2053-1583/aa57fd.

[7] K. L. Low, Y.-C. Yeo, and G. Liang, "Ultimate Performance Projection of Ultrathin Body Transistor Based on Group IV, III-V, and 2-D-Materials," *IEEE Trans. Electron Devices*, vol. 63(2), pp. 773. 2016. doi: 10.1109/TED.2015.2508815.

[8] M.H., Chiu, H. L. Tang, C. C. Tseng, Y. Han, A. Aljarb, J. K. Huang, Y. Wan, J. H. Fu, X. Zhang, W. H. Chang, D. A. Muller, T. Takenobu, V. Tung, and J. L. Li. "Metal-Guided Selective Growth of 2D Materials: Demonstration of a Bottom-Up CMOS Inverter," *Advanced Materials*, vol. 31(18), p. 1900861. 2019. doi: 10.1002/adma.201900861

[9] D. K. Polyushkin, S. Wachter, L. Mennel, M. Paur, M. Paliy, G. Iannaccone, G. Fiori, D. Neumaier, B. Canto & T, Mueller "Analogue two-dimensional semiconductor electronics," *Nature Electronics*, vol. 3, pp. 486–491. 2020. doi: 10.1038/s41928-020-0460-6

[10] C. McAndrew, "Practical Modeling for Circuit Simulation," *IEEE J. Solid-State Circ.*, vol. 33(3), pp. 439-448. 1998. doi: 10.1109/4.661209.

[11] A. V. Penumatcha, R. B. Salazar, and J. Appenzeller, "Analysing black phosphorus transistors using an analytic Schottky barrier MOSFET model," *Nature Communications*, vol. 6, pp. 8948-1-8948-8. 2015. doi: 10.1038/ncomms9948.

[12] A. Prakash, H. Ilatikhameneh, P. Wu and J. Appenzeller, "Understanding Contact Gating in Schottky Barrier Transistors from 2D Channels," *Sci. Rep.*, vol. 7(1) pp. 1-9. 2017, doi: 10.1038/s41598-017-12816-3.

[13] I. Bejenari, M. Schröter, and M. Claus, "Analytical Drain Current Model of 1-D Ballistic Schottky-Barrier Transistors," *IEEE Trans. Electron Devices*, vol. 64(9) pp. 3904-3911. 2017, doi: 10.1109/TED.2017.2721540

[14] R. Landauer, "Spatial variation of currents and fields due to localized scatterers in metallic conduction," *IBM J. Res. Develop.*, vol. 1(3), pp. 223-231. 1957, doi: 10.1147/rd.13.0223.

[15] W. Cao, J. Kang, W. Liu, and K. Banerjee, "A compact current–voltage model for 2D semiconductor based field-effect transistors considering interface traps, mobility degradation, and inefficient doping effect," *IEEE Trans. Electron Devices*, vol. 61(12), pp. 4282-4290.. 2014, doi: 10.1109/TED.2014.2365028.

[16] D. Jiménez, "Drift-diffusion model for single layer transition metal dichalcogenide field-effect transistors," *Appl. Phys. Lett.*, vol. 101(24), pp. 243501-1-243501-4, 2012., doi: 10.1063/1.4770313.

[17] L. Wang, S. Peng, W. Wang, G. Xu, Z. Ji, N. Lu, L. Li, Z. Jin, and M. Liu, "Surface-potential-based physical compact model for graphene field effect transistor," *J. Appl. Phys.*, vol. 120, pp. 084509-1 - 084509-6. 2016. doi: 10.1063/1.4961609.

[18] E. Yarmoghaddam, N. Haratipour, S. J. Koester, and S. Rakheja, "A Physics-Based Compact Model for Ultrathin Black Phosphorus FETs - Part I: Effect of Contacts, Temperature, Ambipolarity, and Traps," *IEEE Trans. Electron Devices*, vol. 67(1) pp. 389-396, Jan. 2020, doi: 10.1109/TED.2019.2951662.

[19] H. Wang, A. Hsu, J. Kong, D. A. Antoniadis, and T. Palacios, "Compact Virtual-Source Current–Voltage Model for Top- and Back-Gated Graphene Field-Effect Transistors," *IEEE Trans. Electron Devices*, vol. 58(5), pp. 1523-1533. 2011. doi: 10.1109/TED.2011.2118759

[20] G. M. Landauer, D. Jiménez, and J. L. González, "An Accurate and Verilog-A Compatible Compact Model for Graphene Field-Effect Transistors," *IEEE Trans. Nanotechnol.*, vol. 13(5), pp. 895-904. 2014doi: 10.1109/TNANO.2014.2328782

[21] Y. Taur, J. Wu, and J. Min, "A Short-Channel I-V Model for 2-D MOSFETs," *IEEE Trans. Electron Devices*, vol. 63(6) pp. 2550-2555. 2016. doi: 10.1109/TED.2016.2547949.

[22] J. Cao, S. Peng, W. Liu, Q. Wu, L. Li, D. Geng, G. Yang, Z. Ji, N. Lu, and M. Liu, "A new surface-potential-based compact model for the $MoS_2$ field effect transistors in active matrix display applications," *J. Appl. Phys.*, vol. 123, pp. 064501-1 - 064501-8. 2018. doi: 10.1063/1.5011794.

[23] S. V. Suryavanshi, and E. Pop, "S2DS: Physics-based compact model for circuit simulation of two-dimensional semiconductor devices including non-idealities," *J. Appl. Phys.*, vol. 110(22), pp. 224503-1 - 224503-10. 2016. doi: 10.1063/1.4971404.

[24] C. Yadav, A. Agarwal, and Y. S. Chauhan, "Compact Modeling of Transition Metal Dichalcogenide based Thin body Transistors and Circuit Validation," *IEEE Trans. Electron Devices*, vol. 64(3), pp. 1322-1329. 2017. doi: 10.1109/TED.2016.2643698.

[25] B. Das and S. Mahapatra, "An atom-to-circuit modeling approach to all-2D metal-insulator-semiconductor field-effect transistors," *npj 2D Mater. Appl.*, vol. 2(1), pp. 28–38. 2018. doi: 10.1038/s41699-018-0073-3.

[26] F. Pasadas, E. G. Marin, A. Toral-Lopez, F.G. Ruiz, A. Godoy, S. Park, D. Akinwande, & D, Jiménez. "Large-signal model of 2DFETs: compact modeling of terminal charges and intrinsic capacitances". vol. 3, pp. 47. *Npj 2D Materials and Applications*. 2019. doi: 10.1038/s41699-019-0130-6.

[27] C. Yadav, P. Rastogi, T. Zimmer, and Y. S. Chauhan, "Charge-Based Modeling of Transition Metal Dichalcogenide Transistors Including Ambipolar, Trapping, and Negative Capacitance Effects," *IEEE Trans. Electron Devices*, vol. 65(10), pp. 4202-4208. 2018. doi: 10.1109/TED.2018.2855109.

[28] L. Wang, Y. Li, X. Feng, K.-W. Ang, X. Gong, A. Thean, and G. Liang, "A unified surface potential based physical compact model for both unipolar and ambipolar 2D-FET: Experimental verification and circuit demonstration," *Proc. IEEE Int. Electron Devices Meeting*, pp. 31.4.1-31.4.4. 2017. doi: 10.1109/IEDM.2017.8268481.

[29] E. G. Marin, S. J. Bader, and D. Jena, "A New Holistic Model of 2-D Semiconductor FETs," *IEEE Trans. Electron Devices*, vol. 65, no. 3, pp. 1239-1245, Mar. 2018, doi: 10.1109/TED.2018.2797172.

[30] D. Yin, A. AlMutairi, and Y. Yoon, "Assessment of High-Frequency Performance Limit of Black Phosphorus Field-Effect Transistors," *IEEE Trans. Electron Devices*, vol. 64, no. 7, pp. 2984-2991, 2017, doi: 10.1109/TED.2017.2699969.

[31] R. M. Corless, G. H. Gonnet, D. E. G. Hare, D. J. Jeffrey, and D. E. Knuth, "On the Lambert-W function," *Adv. Comput. Math.*, vol. 5, no. 1, pp. 329-359, 1996, doi: 10.1007/BF02124750.

[32] S. A. Ahsan, S. K. Singh, C. Yadav, E. G. Marín, A. Kloes and M. Schwarz, "A Comprehensive Physics-based Current-Voltage SPICE Compact Model for 2D-Material-based Top-contact Bottom-gated Schottky-Barrier FETs," *IEEE Trans. Electron Devices*, vol. 67, no. 11, pp. 5188-5195, 2020. doi: 10.1109/TED.2020.3020900.

[33] P. Sebah and X. Gourdon, "Newton's method and high order iterations," *Numbers Comput.*, vol. 1, no. 10, pp. 1–10, 2001 [Online] Available: http://old.sztaki.hu/bozoki/oktatas/nemlinearis/SebahGourdon-Newton.pdf.

[34] A. S. Householder, *Numerical Treatment of a Single Nonlinear Equation*, New York, NY, USA: McGraw-Hill, 1973.

[35] K. K. H. Smithe, C. D. English, S. V. Suryavanshi, and E. Pop, "High-Field Transport and Velocity Saturation in Synthetic Monolayer $MoS_2$," *Nano Lett.*, vol. 18, pp. 4516-4522, 2018. doi: 10.1021/acs.nanolett.8b01692.

[36] S. Salahuddin, and S. Datta, "Use of negative capacitance to provide voltage amplification for low power nanoscale devices" *Nano Letters*, vol. 8, no. 2, pp. 405-410. 2008. doi: 10.1021/nl071804g

[37] M. Si, C.-J. Su, C. Jiang, N. J. Conrad, H. Zhou, K. D. Maize, G. Qiu, C.-T. Wu, A. Shakouri, M. A. Alam, and P. D. Ye, "Steep-slope hysteresis-free negative capacitance MoS2transistors," *Nature Nanotechnol.*, vol. 13, no. 1, pp. 24-28. 2018. doi: 10.1038/s41565-017-0010-1.

[38] H. Lee, Y. Yoon, and C. Shin, "Current-voltage model for negative capacitance field-effect transistors," *IEEE Electron Device Lett.*,vol. 38, no. 5, pp. 669–672. 2017. doi: 10.1109/LED.2017.2679102.

[39] S. Alghamdi, M. Si, L. Yang, and P. D. Ye, "Low frequency noise in MOS2 negative capacitance field-effect transistor," *Proc. IEEE Int. Rel. Phys. Symp. (IRPS)*, pp. P-TX.1-1–P-TX.1-5. 2018. doi: 10.1109/IRPS.2018.8353696.

[40] H. Xu, S. Fathipour, E. W. Kinder, A. C. Seabaugh, and S. K. F. Shirey, "Reconfigurable Ion gating of 2H-MoTe2 field-effect transistors using poly(ethylene oxide)-$CsClO_4$ solid polymer electrolyte," *ACS Nano.*, vol. 9(5), pp. 4900-4910. 2015. doi: 10.1021/nn506521p.

[41] E. Yarmoghaddam, N. Haratipour, S. J. Koester, and S. Rakheja, "A Physics-Based Compact Model for Ultrathin Black Phosphorus FETs - Part II: Model Validation Against Numerical and Experimental Data," *IEEE Trans. Electron Devices*, vol. 67(1) pp. 397-405, Jan. 2020, doi: 10.1109/TED.2019.2955651.

[42] N. Haratipour, S. Namgung, S. H. Oh, and S. J. Koester, "Fundamental limits on the subthreshold slope in Schottky source/drain black phosphorus field-effect transistors," *ACS Nano.*, vol. 10, no. 3, pp. 3791-3800, Feb. 2016, doi: 10.1021/acsnano.6b00482.

[43] C. C. McAndrew, "Validation of MOSFET model Source-Drain Symmetry," *IEEE Trans. Electron Devices*, vol. 53, no. 3, pp. 2202-2206. 2006. doi: 10.1109/TED.2006.881005.